2022 EAGE ANNUAL
83RD CONFERENCE & EXHIBITION
MADRID I SPAIN

# PS IMAGING ON THE EDVARD GRIEG FIELD: APPLICATION OF PS REFLECTION FWI AND FWI IMAGING

M. Peiro[1], W. Gao[1], A. Fotsoh[1], N. Masmoudi[1], A. Roodaki[1], A. Ratcliffe[1], H. Prigent[1], O. Leblanc[1], P.E. Dhelie[2], V. Danielsen[2], J.A. Haugen[2], K.R. Straith[2]

[1] CGG; [2] Lundin Energy Norway

## Summary

Multi-component data recording from ocean-bottom seismic (OBS) surveys captures both PP and PS (converted wave) events. Processing such data can produce superior images compared to those obtained from conventional streamer acquisitions. In addition, PP and PS images can provide valuable insights into reservoir properties. However, PS imaging needs high-quality and high-resolution P- and S-wave velocity models in depth. While full-waveform inversion (FWI) for P-wave velocity model building is well established, an equivalent tool for updating the S-wave velocity (Vs) is still a challenge. A recent FWI methodology based on PS reflection data (PS-RFWI) has been proposed for the Vs model building. Updates from this technique are typically low wavenumber in nature. In this abstract, we show an application of PS-RFWI to OBS data from the Central North Sea and demonstrate an approach to update the high-wavenumber Vs components. Our real data application produces a high-quality 30 Hz Vs model that reduces the image undulations at the reservoir level and allows to generate a subsequent high-resolution Vs FWI Image.

# PS imaging on the Edvard Grieg field: application of PS Reflection FWI and FWI Imaging

## Introduction

Ocean-bottom seismic (OBS) acquisitions record wide-azimuth data with long offsets that are useful for velocity model building with full-waveform inversion (FWI). By recording multi-components, OBS acquisitions capture both the PP and PS (converted wave) events. Subsequent PP and PS data processing can provide valuable insights into reservoir characterization and monitoring. The quality of PP imaging depends mainly on the P-wave velocity ($V_P$) model accuracy. Current computational capacity enables us to produce high-resolution $V_P$ FWI models with frequencies exceeding 50 Hz (Salaun et al., 2021). These high-resolution FWI models improve the imaging of structures from shallow to deep and provide a direct estimate of the PP reflectivity through FWI Imaging (Zhang et al., 2020).

In addition to the $V_P$ model, PS imaging requires an accurate S-wave velocity ($V_S$) model. Conventional $V_S$ model building from PS reflection data relies on PS (or joint PP-PS) tomography and event registration. It is limited to updating the background, low-wavenumber, $V_S$ model. To reach higher resolution, full-wave based methods are necessary. Elastic FWI would be the most accurate approach, but it remains difficult due to the computational cost of elastic full-wave modeling. As an alternative, quasi-elastic Born modeling can be used (Feng and Schuster, 2019). In this approach, the PS reflected wave field is approximated by a formula using acoustic wavefields propagating in the $V_P$ and $V_S$ background models. Based on an approximation to this quasi-elastic Born modeling, Masmoudi et al. (2021) proposed an adaptation of reflection-FWI (RFWI; Xu et al., 2012) to PS data, which allows the background Vs model to be updated. An advantage of the approach was that the perturbation model was derived from the PP-reflectivity and then fixed during the non-linear iterations to avoid the traditional reflectivity-velocity coupling issue of RFWI (Baina and Valensi, 2018).

Here, we present an application of the PS-RFWI work presented by Masmoudi et al. (2021) over the Edvard Grieg field for the low-wavenumber update of the $V_S$ model. In addition, high-wavenumber components are recovered through a PS-FWI, opening the door to "$V_S$ FWI Imaging" in order to replicate the benefits on PS data to those observed in "$V_P$ FWI Imaging" of PP data.

## Edvard Grieg field, Central North Sea

Edvard Grieg is an oil field discovered in the Central North Sea in 2007, located in the Utsira High area. The reservoir interval is thin, less than 50 m, and located beneath a high-impedance chalk layer. Very strong vertical and lateral velocity contrasts make imaging and reservoir characterization challenging. The application of high-end technologies, such as state-of-the-art data processing and high-resolution FWI for $V_P$ model building, to a recent OBS acquisition can help overcome some of these challenges.

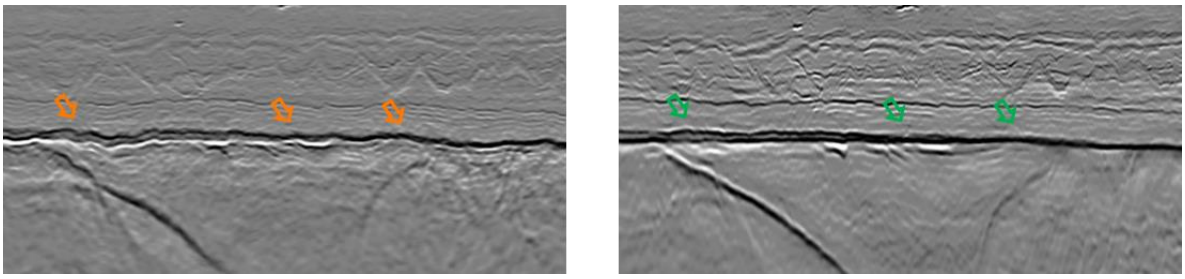

***Figure 1.*** *Comparison of legacy PP Kirchhoff pre-stack depth migration (left) and 65 Hz $V_P$ FWI Image (right). The latter improves the flatness of the chalk (indicated by the arrows) and the reservoir below.*

In this field, we used Time-Lag FWI (TLFWI; Zhang et al., 2018) to invert for a 65 Hz $V_P$ model, with this frequency incorporating the dominant data bandwidth. A direct derivation of the subsurface reflectivity is possible with such a highly detailed velocity model through FWI Imaging (Zhang et al., 2020), which proved a superior tool for reconciling the seismic image with well log measurements and

drilling observations. The flatness of the top chalk was much improved compared to all previous model building and imaging methods (Figure 1), as was the reservoir depth immediately below this horizon.

**PS-Born approximation and gradients of PS-FWI**

In our PS-FWI methodology, PS-reflection data are modeled using a modified quasi-elastic Born approximation (Masmoudi et al., 2021). Based on the scale separation assumption of the Born approximation, the S-wave velocity model, $V_S$, is divided into a low-wavenumber background model, $V_{0_S}$, and a high-wavenumber perturbation model, $\delta V_S$. The low-wavenumber and high-wavenumber P-wave velocity models, $V_{0_P}$ and $\delta V_P$, are derived in a previous step from the pressure component only.

PS-RFWI, as proposed by Masmoudi et al. (2021), is applied as an adaption of RFWI (Xu et al., 2012; Gomes and Chazalnoel, 2017) to PS reflection data. In standard RFWI, the background and perturbation velocity models are updated using FWI approaches, which minimize the difference between the observed and modeled PS data by optimization of an objective function $J$. This objective function can be the usual least-squares data difference, or one of the newer cost functions that can accommodate some amplitude differences between observed and modeled data, for example, Time-Lag (Zhang et al., 2018) or Partial Matching (Cooper et al., 2021). The FWI gradients for the background $V_{0_S}$ and the perturbation $\delta V_S$ models can be efficiently obtained via the adjoint-state method, as follows:

$$\frac{\partial J}{\partial V_{0_S}} = \int_{t=0}^{tmax} \frac{\partial \delta S(t)}{\partial V_{0_S}} R(t)\, dt, \qquad (1)$$

$$\frac{\partial J}{\partial \delta V_S} = \int_{t=0}^{tmax} -\frac{\partial^2 P(t)}{\partial t^2} R(t)\, dt, \qquad (2)$$

where $\delta S$ is the scattered S-wavefield propagating in the background $V_{0_S}$ model, $P$ is the incident P-wavefield propagating in the background $V_{0_P}$ model, and $R$ is the adjoint S-wavefield obtained by backpropagating the residuals of the PS-reflection data injected at the receiver positions.

An alternative update of both $V_{0_S}$ and $\delta V_S$ is very challenging due to the crosstalk between the two parameters, potentially leading to slow convergence (Baina and Valensi, 2018). Hence, in the first step, $V_{0_P}$ is assumed accurate, and $\delta V_P$ is used to form a fixed reflectivity model which avoids the traditional reflectivity-velocity coupling issue of RFWI. Thus, only $V_{0_S}$ is updated using the "single-sided rabbit-ear" tomographic-like term in equation 1 (Masmoudi et al., 2021). This background model describes the kinematics of the scattered PS-wave events. In the second step, we propose to also update the perturbation $\delta V_S$ model through the migration-like term in equation 2, which is a more conventional approach of FWI using reflections, those reflections being generated by Born modeling with the perturbation model. This perturbation model is subsequently combined with the background $V_{0_S}$ model to form the final, high-resolution, $V_S$ model. A form of PS-reflectivity can be then built by $V_S$ FWI Imaging taking the spatial derivative of the final $V_S$ model along the normal to the reflector plane.

**Application and results on Edvard Grieg**

The input seismic data to PS-RFWI consisted of recently processed radial component, PS-reflection gathers from an OBS acquisition in 2018. PS-RFWI requires isolating PS-reflection events only, which can be difficult with field data. Hence, we applied designature, demultiple and source-side deghosting to the data. We used a total of 34 receiver lines (9087 nodes) over the main Edvard Grieg area for the $V_S$ update. We also selected 3 wells with good quality shear sonic logs over a large vertical interval as calibration points to the starting model and for QC of the PS-RFWI updates. The stratigraphic model consisted of 8 interpreted horizons in depth, from water bottom down to top chalk. The starting $V_S$ model for PS-RFWI was built from various sources of information: a smoothed and edited version of the TLFWI $V_P$ model, information from the P- and S-sonic logs, a multi-wave inversion (Bardainne, 2018), and a PP-PS registration between the water bottom and the first interpreted horizon (around 200 m depth). The $V_S$ model was then updated in two steps: first, the background $V_{0_S}$ model and, second, the

high-resolution perturbation $\delta V_S$ model. The perturbation $\delta V_S$ update was then combined with the background $V_{0_S}$ model to obtain the final $V_S$ model that should correct for kinematics and depthing of events as well as contain high-resolution features.

Figure 2 compares the starting $V_S$ model, updated background $V_{0_S}$ model (at 8 Hz), and fully updated $V_S$ model as well as the corresponding image sections. The updated $V_S$ model (top right panel) highlights rich vertical and lateral details consistent with the main geological features visible on the seismic sections. Further, we can clearly see the improvement achieved by the background PS-RFWI update in flattening and focusing at the depth of the chalk horizon (green line) on the converted-wave reverse time migration (PS-RTM) images (bottom left and middle panels, both at 30 Hz). The $V_S$ FWI Image that we derived from the final $V_S$ model (bottom right panel) also reaches 30 Hz and provides a high-resolution and geologically consistent section from the overburden to the top chalk, which appears much flatter. At reservoir level, we see improved signal-to-noise ratio and illumination thanks to the PS-LSRTM like process embedded in the PS-RFWI algorithm. A comparison of the $V_S$ FWI Image with the legacy PS-RTM section (Figure 3) shows how this new workflow achieves similar improvements in the PS data, as was observed in the $V_P$ FWI Image (Figure 1).

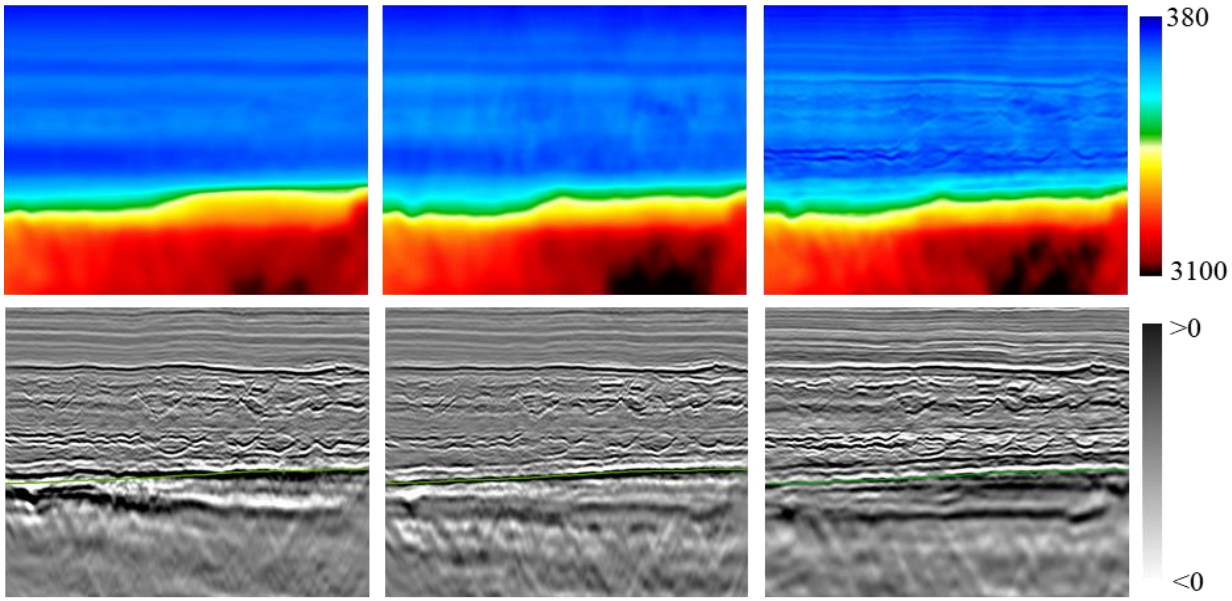


***Figure 2*** *Top: section comparisons of $V_S$ models: starting (left), background $V_{0_S}$ model update (middle), and combined background $V_{0_S}$ and perturbation $\delta V_S$ models (right). Bottom: 30 Hz section comparisons of: PS-RTM migrated with starting model (left), PS-RTM migrated with background $V_{0_S}$ model update (middle), and Vs FWI image (right). The green line on the lower sections indicates the PP chalk horizon.*

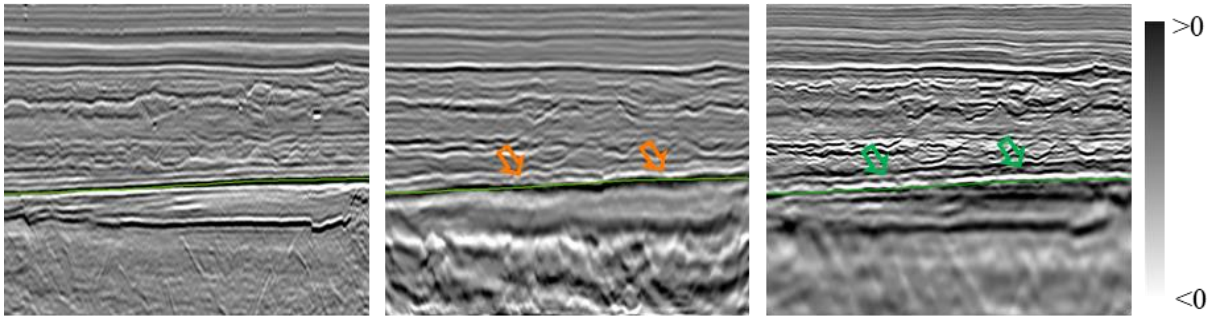


***Figure 3*** *Comparison of $V_P$ FWI Image filtered to 30 Hz (left), legacy 30 Hz PS-RTM (middle), and 30 Hz $V_S$ FWI Image (right). The latter improves the flatness of the chalk (arrows) and the reservoir below, matching with the PP data.*

## Discussion

Here our PS-reflections are attributed to rough perturbations in $V_S$ only via the Born approximation's scale separation, with such scale separation unlikely to be perfect. Further, the inverted $\delta V_S$ model may have leakage from the density, as PS-reflection coefficients depend on both $V_S$ and density contrasts. A pragmatic way to mitigate these issues is to scale the inverted perturbation $\delta V_S$ model before combining with the background $V_{0\,S}$. This scaling parameter can be calibrated, for example, with well-logs or FWI-guided tomography (Allemand et al., 2019). If we obtain an accurate calibration, then a benefit of this approach over a least-squares PS-RTM is that the $V_S$ FWI Image will also contain the low-wavenumber contribution from the background model, whereas the least-squares PS-RTM will not. Finally, while a full elastic FWI is still the end goal, there is associated extra cost and complexity: our proposed methodology is more cost effective than elastic FWI. However, we still must honor the minimum $V_S$ velocity needed for accurate S-wave propagation, here being ~250 m/s in the shallow section.

## Conclusions

Using an appropriately processed OBS data set and a successful $V_p$ TLFWI model build with subsequent $V_p$ FWI Image, we produced a high-quality $V_s$ model over the Edvard Grieg area that reduces image undulations at the reservoir level and can support reservoir characterization. The proposed PS-RFWI approach was cost-effective, giving high-wavenumber updates and a $V_s$ FWI Image to 30 Hz.

## Acknowledgements

We would like thank Lundin Energy Norway and their partners in PL338, Wintershall Dea and OMV, and CGG for permission to publish this work. We also thank Gilles Lambaré for valuable discussions.

## References

Allemand, T., Lopes, L., Lambaré, G. and Leblanc, O. [2019], High resolution Full Waveform Inversion: Two Pitfalls and a Remedy. *81st EAGE Conference & Exhibition*, Extended Abstracts, Tu R08 07.

Baina, R. and Valensi, R. [2018] Borrowing insight from travel-time reflection tomography to solve the depth reflectivity-velocity coupling issue of RFWI. *80th EAGE Conference & Exhibition*, Workshop Programme, WS01.

Bardainne, T. [2018], Joint inversion of refracted P-waves, surface waves and reflectivity. *80th EAGE Conference & Exhibition*, Extended Abstracts, We K 02.

Cooper, J., Ratcliffe, A. and Poole, G. [2021] Mitigating cycle skipping in full-waveform inversion using partial matching filters. *82nd EAGE Conference & Exhibition*, Extended Abstracts.

Feng, Z. and Schuster, G. [2019] True-amplitude linearized waveform inversion with the quasi-elastic wave equation. *Geophysics*, *84*(6), 827-844.

Gomes, A. and Chazanoel, N. [2017] Extending the reach of FWI with reflection data: Potential and challenges. *87th Annual International Meeting, SEG*, Expanded Abstracts, 1454-1459.

Masmoudi, N., Ratcliffe, A., Wang, M., Xie, Y. and Wang, T. [2021] A practical implementation of converted-wave reflection full-waveform inversion. *82nd EAGE Conference & Exhibition*, Extended Abstracts.

Salaun, N., Reinier, M., Espin, I. and Gigou, G. [2021] FWI velocity and imaging: A case study in the Johan Castberg area. *82nd EAGE Conference & Exhibition*, Extended Abstracts.

Xu, S., Chen, F., Lambaré, G., Zhang, Y. and Wang. D. [2012] Inversion on reflected seismic wave. *82nd Annual International Meeting, SEG*, Expanded Abstracts.

Zhang, Z., Mei, J., Lin, F., Huang, R. and Wang, P. [2018] Correcting for salt misinterpretation with full waveform inversion. *88th Annual International Meeting, SEG*, Expanded Abstracts, 143-1147.

Zhang, Z., Wu, Z., Wei, Z., Mei, J., Huang, R. and Wang, P. [2020] FWI Imaging: Full-wavefield imaging through full-waveform inversion. *90th Annual International Meeting, SEG*, Expanded Abstracts, 656- 660.